Pergamon

PII: S0148-9062(98)00165-X

Int. J. Rock Mech. Min. Sci. Vol. 35, No. 8, pp. 1051–1070, 1998

Printed in Great Britain
0148-9062/98 $ - see front matter

Effect of Shear Displacement on the Aperture and Permeability of a Rock Fracture

I. W. YEO†
M. H. DE FREITAS‡
R. W. ZIMMERMAN†

The results of experiments using radial and unidirectional flow in a carefully described single rough aperture are reported and compared with numerical predictions. Aperture replicas of a natural sandstone fracture were made at 0, 1 and 2 mm shear displacements using silicone rubber, with a reproducibility of better than 2%. The experimental arrangement permitted shear displacement to be obtained without causing damage to the two displaced surfaces, which thus retained their original (and essentially matching) geometry. Both the number of contact points and the fractional contact area decreased with increasing shear displacement. With increasing shear displacement, mean aperture and standard deviation increased and the ratio of standard deviation to mean aperture increased slightly. Semivariogram studies indicated that as shear displacement increased in the direction normal to the roughness ridges, the aperture distribution became more closely correlated in the direction parallel to the roughness ridges than in the shear direction. Flow tests showed that with increasing shear displacement, the fracture became heterogeneous and anisotropic and became more permeable in the direction perpendicular to the shear displacement than in the direction parallel to the displacement. Simulations were made of flow through the fracture using the Reynolds equation and the actual aperture distribution; the measured hydraulic apertures were generally about 20% lower than those measured numerically. © 1998 *Elsevier Science Ltd. All rights reserved*

INTRODUCTION

The hydraulic and mechanical properties of rock fractures are of considerable interest in several areas of rock engineering, such as near-field modelling of hydraulic processes around radioactive waste repositories [1–3], underground tunnels [4, 5] and storage caverns [6], rock slope stability [7], petroleum and geothermal reservoirs [8] and solute transport [9]. Rock features such as single fractures, faults or a fracture network can greatly influence the hydrological properties of rock masses and control the mechanical behaviour of rock masses as well. Flow through a single rock fracture is the basic building block of realistic models of fluid flow in rock fracture networks.

Fluid flow through rock fractures has traditionally been described by the cubic law, which follows from the assumption that the fracture consists of the region bounded by two smooth, parallel plates [10]. Real rock fractures, however, have rough walls and variable apertures, as well as asperity regions where the two opposing faces of the fracture walls are in contact with each other. The hydraulic conductivity of a rock fracture depends on the aperture distribution, surface roughness and contact area, all of which are functions of the stress that acts on the fracture plane. In recent years, numerous theoretical, numerical and experimental studies have investigated the effect of variable apertures and asperity geometry on fluid flow through a fracture [11–18]. The effect of stress on the conductivity of a rock fracture has been studied by, among others, Walsh [19], Barton *et al.* [20], Pyrak-Nolte *et al.* [21] and Olsson and Brown [22]. Despite much recent work, a complete understanding of the relationship between void space geometry, applied stress and hydraulic conductivity has yet to be achieved. The difficulties lie in the intractability of the Navier–Stokes equations that govern fluid flow through the fracture,

†Department of Earth Resources Engineering, Imperial College of Science, Technology and Medicine, London SW7 2BP, U.K.
‡Department of Civil Engineering, Imperial College of Science, Technology and Medicine, London SW7 2BP, U.K.

incomplete knowledge of the details of the fracture geometry and a lack of realistic constitutive relations governing the mechanical deformation of rough rock surfaces in partial contact.

Although *in situ* rock fractures are subject to both normal and shear loading (in particular, rock fractures around the periphery of underground openings experience severe shearing) most previous laboratory investigations have considered only normal stress effects [21, 23–25]. Only a few studies have been conducted for investigating the effect of shear displacement on fluid flow through single rock fractures, among which are those by Makurat *et al.* [14], Olsson and Brown [22], Esaki *et al.* [17] and Gentier *et al.* [26]. In addition, despite the fact that many rock fractures have anisotropic flow properties, none of these studies have been dedicated to the issue of flow anisotropy by shearing, except that of Gentier *et al.* [26].

In the present work, a test device has been developed that utilises "boreholes" as injection or monitoring holes to determine the directional hydraulic properties of a fracture through radial flow tests. The apparatus has been designed to also allow water to flow in two mutually perpendicular directions along the plane of the fracture. The design of the apparatus allows for measurements to be made under different normal load and shear displacement states. The variation of aperture and contact distribution was examined at various levels of shear displacement. Numerical simulations have also been conducted using the measured aperture field, for comparison with the experimental results.

EXPERIMENTAL SYSTEM

Rock fracture replicas

Rock fracture replicas were made from epoxy resin, using a natural rock fracture in a red Permian sandstone, the surface of which could be seen to have anisotropic roughness. The ridges of roughness were aligned along the "x" direction. The first replica was made by copying the rock surface using Silcoset, which is a liquid silicone rubber that cures to form a resilient, solid silicone rubber with the addition of curing agents (Fig. 1). This silicone rubber replica (Silcoset 1) was used as a mould for the epoxy resin casting (epoxy 1), which became the lower half of the fracture. In order to make a matching opposite surface, the surface of the first resin replica was copied using Silcoset (Silcoset 2) and this surface was copied again using Silcoset (Silcoset 3). The third Silcoset replica was used as a mould for the epoxy resin casting (epoxy 2), which became the upper half of rock fracture. The two epoxy resin replicas, when fitted together, formed matching copies of the natural rock fracture (Fig. 1). A square replica of each surface of the rock fracture was made, 1 cm larger in size than that of the fracture used in experiments, 21 cm, so that each could be cut to fit the shear boxes.

The Silcoset 1 mould contained some damage on its surface, at isolated locations, caused by the Silcoset sticking very strongly to the sandstone surface. These locations were repaired by putting fine-grained sand into the damaged areas, which attached itself to the epoxy 1. These irregularities were filed to match the real surface. Due to this repair work, the two surfaces are not exactly matched, making the fracture have larger apertures (even at zero shear displacement) than those found in the actual fracture. Elsewhere, the rock surface was perfectly copied by the Silcoset and epoxy resin, and the rock fracture replicas resembled the real rock surface. Typical roughness profiles were measured along the x and y direction on surface of the lower half of rock fracture (Fig. 2). Since the ridges are aligned in the x direction, profiles in the y direction are rougher than those in the x direction. Visual comparison of the profiles shown in Fig. 2 with the standard profiles defined by Barton *et al.* [20] lead to estimated joint roughness coefficients of about 5 for profiles in the x-direction and about 9 in the y-direction. In our experiments, the fracture was sheared in the y direction, creating more dilation than if shear occurred in the x direction.

Experimental apparatus

The experimental device was designed for a fracture to be subjected to normal loading and shear displacement by placing the fracture in a shear box (Fig. 3). The lower half of the fracture is fixed to the lower half of the shear box and the upper half of the fracture is placed in the upper shear box without being fixed to it, so as to allow the upper half of the fracture to dilate when sheared. In order to accommodate shear displacement and retain a water seal between the lower and upper shear boxes, a rubber hoop belt and rubber plates were installed between them (Fig. 3) and sealed with high-vacuum grease. Silcoset sealant was used to provide a barrier to leakage between the sides of the specimen and the sides of the box.

A loading platform supported on four legs is placed on the upper half of the fracture, designed to apply normal load to the fracture by simply having weights placed on it. Four side plates were fixed to the lower shear box by screws, to precisely locate the position of the upper shear box and to ensure the exact relative location of the rock surfaces and shear boxes during aperture measurements and flow tests. Exact shear displacement of the upper shear box relative to the lower box was required, as this displacement had to be reproduced accurately on a number of occasions. To achieve this, precisely-dimensioned metal gauge blocks are inserted between the side plate and lower shear box and between the side plate and upper shear box on opposite sides, ensuring 0, 1 and 2 mm shear displacement without rotation (refer to Ref. [27] for details).

A drainage groove was cut along the edge of the lower half of the fracture so as to apply uniform hydraulic heads to the side of the fracture for the uni-

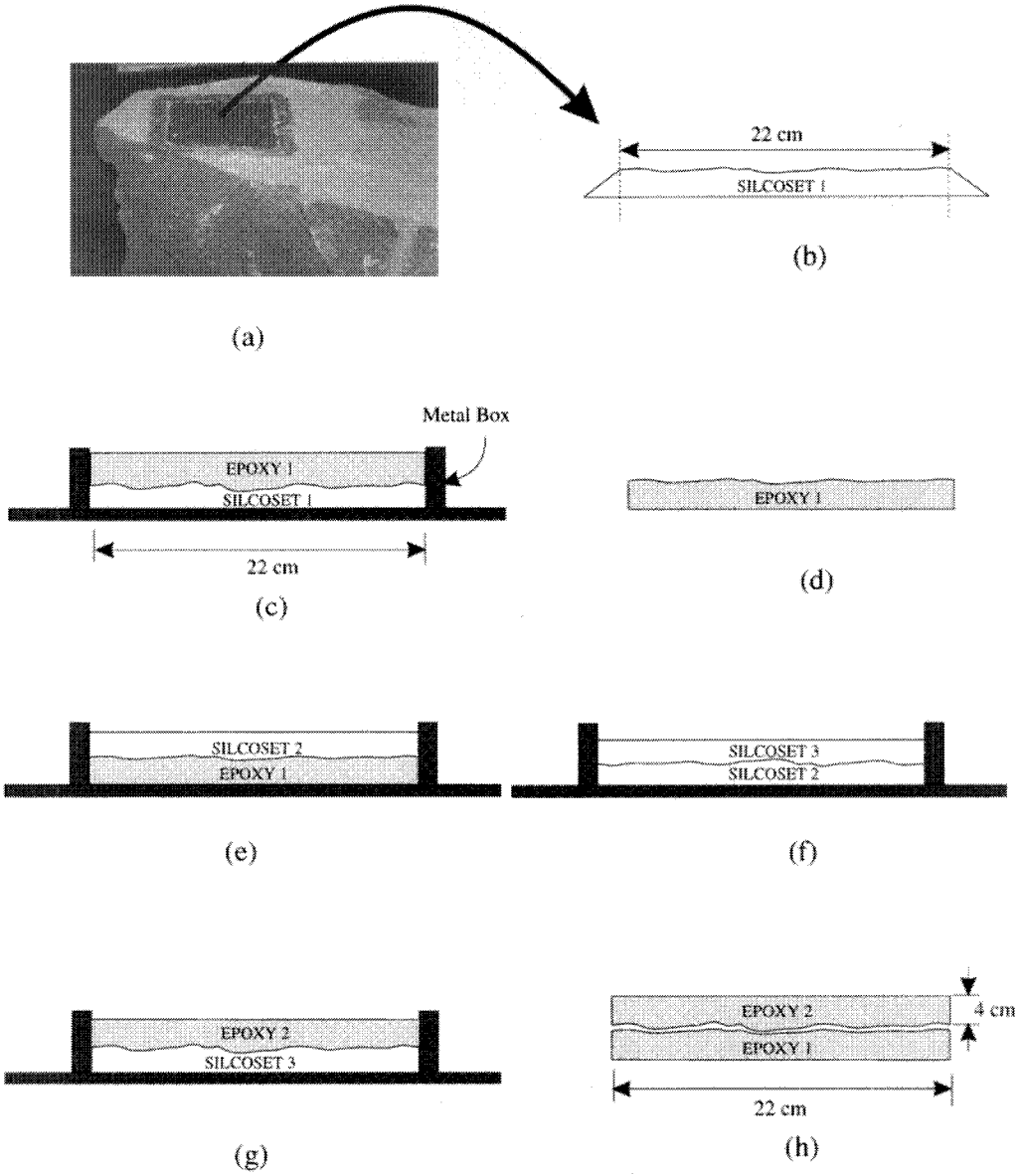

Fig. 1. Process of making rock fracture replicas using Silcoset and epoxy resin.

directional flow tests; the actual size of the fracture in which the fluid flows is 20×20 cm. Thirteen holes of 6 mm diameter were drilled through the upper half of the epoxy resin fracture cast, terminating at the fracture plane, arranged in three concentric circles (Fig. 3). For radial flow tests, the central hole is used as an injection well and the outer holes are used as monitoring wells. For unidirectional flow tests, the central hole is used as a monitoring hole like the others. The hydraulic heads in the injection hole and along the outer boundaries are monitored by manometers and the flowrate is measured by collecting the effluent fluid and measuring its volume as a function of elapsed time.

MEASUREMENT PROCEDURE

Aperture measurement

Methods for aperture measurement were summarised by Hakami [28], who classified them into surface topography, injection and casting methods, each distinguished by a basic measurement procedure. The casting method was adopted for measuring the aperture in this experiment. Silcoset was used to make a replica of the void geometry of the fracture. The aperture replicas were made under a constant normal load, for three different shear displacements: 0, 1 and 2 mm. Shear displacements were applied along the y direction, which is normal to the ridges of roughness. Duplicate aperture replicas were made at the same shear displacement, so as to investigate the reproducibility of the aperture replicas and to verify whether or not the fracture and shear box could be assembled to have exactly the same relative position for both the aperture measurements and the flow tests. The reproducibility of the replicas was measured by comparing their weights, the relative distances between clearly identifiable features on them (such as contact points) and the distribution of lighter and darker regions in the photographs.

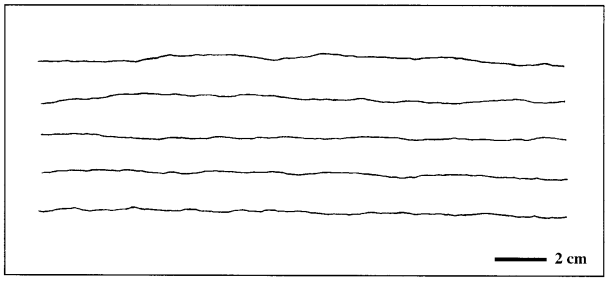

(a) Roughness profiles along the x direction

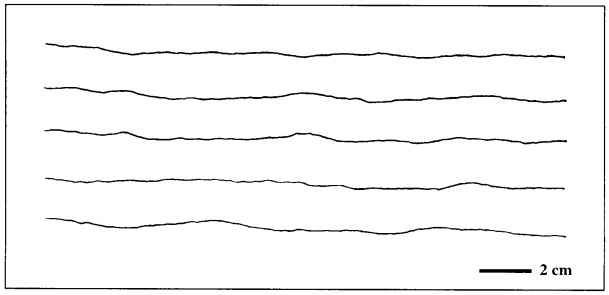

(b) Roughness profiles along the y direction

Fig. 2. Typical roughness profiles of the lower half of the rock fracture used in the experiments. The roughness along the y direction shows a undulating rough profile and that along the x direction is planar rough.

To make a Silcoset cast, the boxes were first positioned accurately using the side plates to ensure the desired amount of shear displacements, during which time the lower specimen was in its lower shear box. Silcoset was then poured on the surface of the lower half of fracture, the upper half of the fracture was placed on the lower surface, and the loading platform was then placed on the upper half of the fracture to apply a normal load of 10 kPa. Monitoring holes and drainage holes were open to allow excess Silcoset to flow out of the fracture. The Silcoset solidified in 24 h. After the rock fracture was separated, the solidified Silcoset replica were removed for study.

Aperture replicas were scanned to determine the void geometry, its spatial distribution and the contact area. Each aperture replica was sliced at 5 mm intervals in the y direction, except in regions close to monitoring holes, into forty strips, which gave aperture profiles along the x direction. Aperture is defined as the vertical thickness at each known (x, y) co-ordinate. Apertures were measured at every 5 mm interval along these sections as a function of location, using the microscope of a "MINILOAD hardness tester" made by Leitz Wetzlar. A micrometer with increments of 1 μm is affixed to the measuring stage, allowing the aperture to be measured to within ± 1 μm. These measurements were carried out at 1600 known x and y co-ordinates for each shear condition. These measured apertures were used as input data for numerical simulations and were also used to calculate the mean and standard deviation of the apertures and to investigate the directional correlation structures.

Flow tests

Radial and unidirectional flow tests were carried out under constant normal load and different shear displacements. Although our apparatus allows different normal loads to be applied, this study focused only on the effect of shear. Since the mechanical behaviour of the epoxy model becomes different from that of a real rock fracture with increasing stress, especially after peak normal and shear stresses have been passed, shear displacements less than that leading to peak shear strength were applied. Bandis *et al.* [29] showed that rock fractures from 5 up to 40 cm in length tended to approach their peak shear stresses when the shear displacement reached about 1% of their overall dimensions. Therefore, in this experiment, the fracture having length of 20 cm was sheared in the y direction, normal to the ridges of roughness, in increments of 1 up to 2 mm, either altering any pre-existing anisotropic transmissivity distribution, or (possibly) creating an anisotropic distribution if the transmissivity was originally isotropic. The same shear offset method was used for all flow tests as was used in making the aperture replicas. After shear displacement was applied to the shear boxes, the upper half of the fracture was placed on the lower half of the fracture through the previously-displaced shear boxes, and then the deadweight normal load of 10 kPa was applied to the fracture.

Unidirectional flow and radial flow tests were performed at shear displacements of 0, 1 and 2 mm. In the radial flow tests, water was injected into the central hole at the upper half of the fracture at constant pressure and flowed out to the outer boundaries that were kept at a constant hydraulic head. Hydraulic heads at the monitoring holes and flowrates into and out of the fracture, were monitored during the radial flow tests. Unidirectional flow tests were conducted along the x and y directions under the same shear displacement as in radial flow tests. For these tests, the drainage groove parallel to the flow direction was closed with plasticine to ensure that fluid flowed only in one direction through the rock fracture. Constant hydraulic heads were applied at the inlet and outlet boundaries and the hydraulic heads and flowrates were measured.

REPRODUCIBILITY OF APERTURE REPLICAS

Table 1 shows the weights of the aperture replicas for different shear displacements. Weight comparisons between duplicate aperture replicas indicated that the replicas were reproduced within less than 2% error and some of this error was due to the precision with which the surplus Silcoset (which existed along the sides and in the monitoring holes) was cut away. Weights were converted into mean apertures using the density of Silcoset, 1.19×10^3 kg/m^3. Mean aperture (measured by weight) was found to increase with increasing shear displacement, as expected. The mean

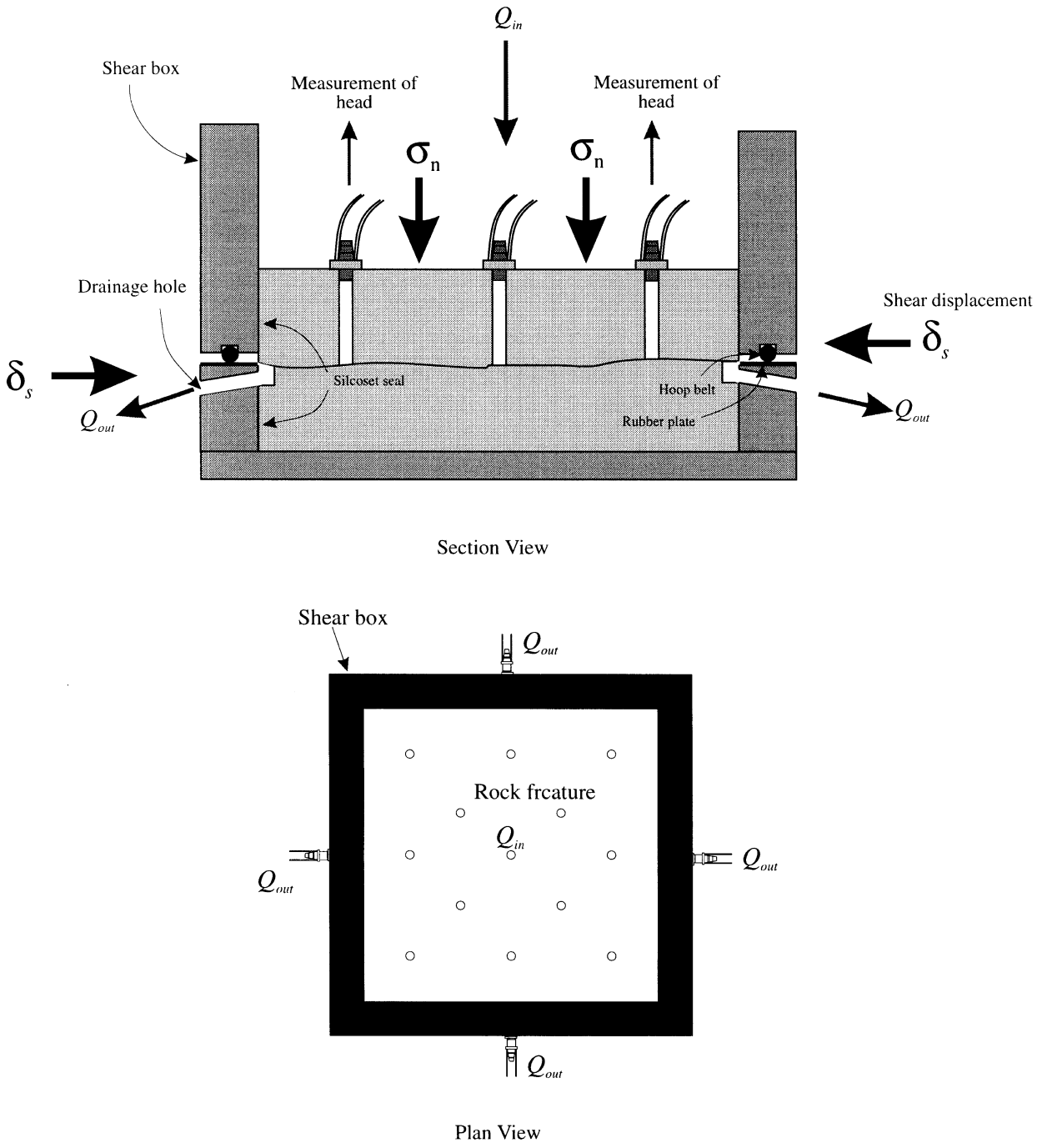

Fig. 3. Schematic diagram of the experimental apparatus.

aperture shows very good agreement with that measured using the microscope.

Aperture replicas were scanned against a black background, using the same brightness and contrast. Because the translucency of Silcoset depends on thickness, contact points are clearly distinguished as black spots and lighter regions correspond to larger aperture. Figure 4 shows scanned photographs of the duplicate aperture replicas after 1 mm shear displacement. In duplicate replicas of each shear condition, shapes of contacts and their relative distances are almost identical (Fig. 4). The distribution of lighter regions, i.e. larger apertures, was very similar between duplicate replicas made at the same shear displacement.

APERTURE DISTRIBUTION

The effect of shear displacement on the distribution of void and contact area was investigated using aperture replicas made under 0, 1 and 2 mm shear displacement (Fig. 5). With increasing shear displacement, the aperture replicas become lighter, indicating that the aperture increases due to dilation of the fracture. At zero shear displacement, larger and smaller apertures are evenly distributed over the fracture, indicating that the fracture is an isotropic medium. The fracture becomes more hydraulically anisotropic with increasing shear displacement, because valleys having smaller apertures exist at the middle of the fracture and also

Table 1. Reproducibility of aperture replicas as estimated by comparing the mean aperture measured under the microscope with the mean aperture measured by total weight for 0, 1 and 2 mm shear displacements. Mean apertures were calculated based on the density of Silcoset, 1.19×10^3 kg/m^3, and their weights. Samples 5, 4 and 7 were used to measure apertures by microscope for 0, 1 and 2 mm of shear displacements, respectively

Shear displacement	Sample	Weight (g)	Mean aperture by weight (μm)	Aperture by microscope (μm)	
				mean	standard dev.
0 mm	1	28.54	599.58		
	5	29.05	610.29	606.55	160.01
1 mm	4	33.87	711.56	711.96	221.23
	8	34.17	717.79		
2 mm	6	47.91	1006.51		
	7	48.84	1026.05	1024.16	331.90

at the northern edge along the direction normal to the shear displacement. The number of contact points and the fractional contact area both decrease as shear displacement increases, although the fractional contact area is too small to quantify. As the aperture replicas were made at a very low normal stress of 10 kPa, it is not surprising that only a few contact points support the fracture (Fig. 5). Iwai [30] showed that the fractional area of the fracture plane that is occupied by contact was 0.001 at 260 kPa of effective normal stress, and increased to the range of 0.1–0.2 at 20 MPa.

Samples 5, 4 and 7 of aperture replicas were selected to measure apertures for 0, 1 and 2 mm shear displacement, respectively. Measured apertures were used as input data to the numerical simulations for comparison with flow test results (see following sections). Figure 6 shows aperture distributions for each shear displacement using the microscopically measured apertures. In general, the void geometries of Fig. 6 at 0, 1 and 2 mm shear displacement, created using measured apertures, show very good agreement with those of the photographs of Fig. 5. Before shear displacement, larger apertures are distributed in the northern and southern regions of the fracture trending in the x direction and along the y direction at the east side of the fracture. Smaller apertures are located at the western and eastern edges, which corresponds to the regions having contact points in Fig. 5.

With increasing shear displacement, larger aperture regions are located at the southern part of the fracture. As observed in Fig. 5, the smaller apertures form the valleys, which trend in the x direction. The fracture becomes inclined towards the north. The fact that there is a relatively large contact point at the southern part (Fig. 5) demonstrates that the upper half of the fracture has not tilted when shear-displaced. (In fact, it should be noted that the boxes and the fracture were not "sheared" as such; the upper box was first displaced over the lower box and its lower surface and then the upper surface lowered into it, so that no shear-induced rotation could occur.) These results suggest that the fracture becomes more anisotropic with regard to fluid flow with increasing shear displacement.

Mean aperture and standard deviation increase with increasing shear displacement, as does the ratio of standard deviation to mean aperture (Table 2). This ratio shows a greater increase from 0 to 1 mm shear displacement than from 1 to 2 mm shear displacement. On the other hand, mean aperture increased sharply when the fracture was shear-displaced from 1 mm and to 2 mm. The difference between minimum and maximum apertures increases as well. The frequency histograms are generally fitted by a normal distribution (Fig. 7). Figure 8 shows aperture profiles along the x direction for each shear displacement. The aperture varies very gradually at all shear displacements, which is a necessary requirement in order to be able to model fluid flow through the fracture using the Reynolds equation (see Section 7). The aperture does change abruptly at some points, but such abrupt changes are very rare [i.e. bottom picture of Fig. 8(b)].

SPATIAL CORRELATION STRUCTURE

Semivariograms have been used to study the spatial correlation structure by Iwano and Einstein [31] and Hakami [28]. Semivariance $\gamma(l)$ is calculated from [32]

$$\gamma(l) = \frac{1}{2n}\sum_{i=1}^{n}[e(x_i) - e(x_{i+l})], \tag{1}$$

where l is the lag distance, n is the number of observation pairs, $e(x_i)$ is the aperture taken at location x_i and $e(x_{i+l})$ is the aperture taken l intervals away. If the lag distance is small, the compared apertures tend to be very similar, consequently leading to small semivariance values. As the apertures being compared move further apart, their correlation with each other decreases and their difference becomes larger, which results in a larger semivariance value. At some lag distance the apertures being compared are too far apart to be correlated with each other and their squared differences become equal in magnitude to the variance of apertures. The sill is defined as a flat level that the semivariogram develops when the semivariance no longer increases. Ideally, the sill is equal to aperture variance. The lag distance at which the semivariance approaches the sill is referred to as the "range" or the "spatial correlation length" and defines a neighbourhood within which all apertures are closely correlated to each other.

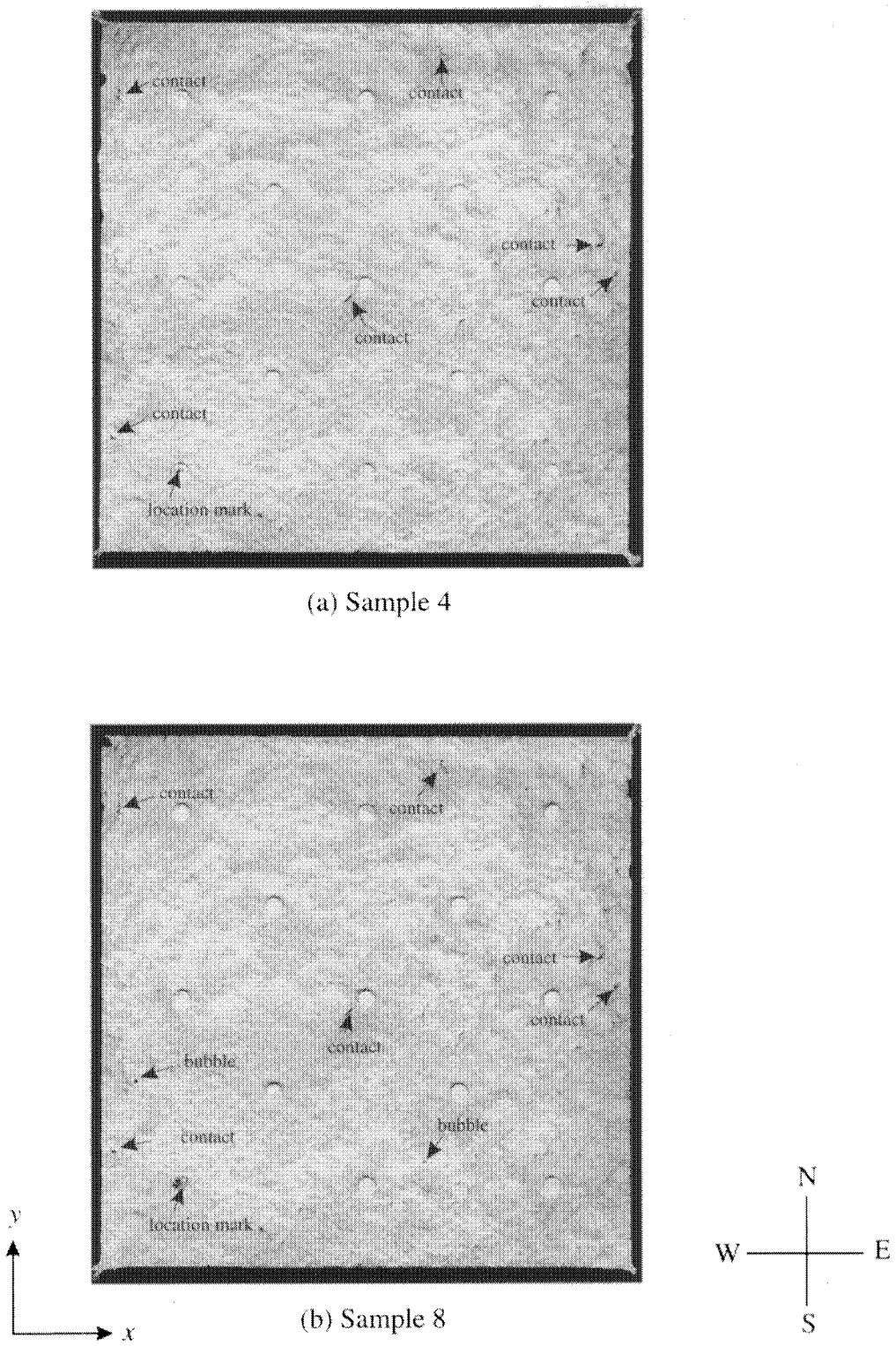

Fig. 4. Duplicate aperture replicas at 1 mm shear displacement to verify reproducibility.

Semivariance was calculated both omnidirectionally and in the x and y directions, for each shear displacement (Fig. 9) using the computer package VARIOWIN [33]. At 0 and 1 mm shear displacements, the semivariograms do not develop clear sills for either the omnidirectional case or the y direction, resulting in difficulties calculating the ranges. Even though the flat sills are weakly developed at the x direction, the high "nugget effect" (whereby the semivariogram does not go through the origin but rather has a non-zero value) obstructs the accurate determination of ranges. The ratio of the value of the nugget effect to the flat sill is over 0.6, suggesting that, although modelled by a semivariogram, more than 60% of the aperture correlation structure is unpredictable [32].

At 2 mm shear displacement, flat sills are seen to develop for all directions. Although the flat plateau is lower than the variance of apertures (shown by the

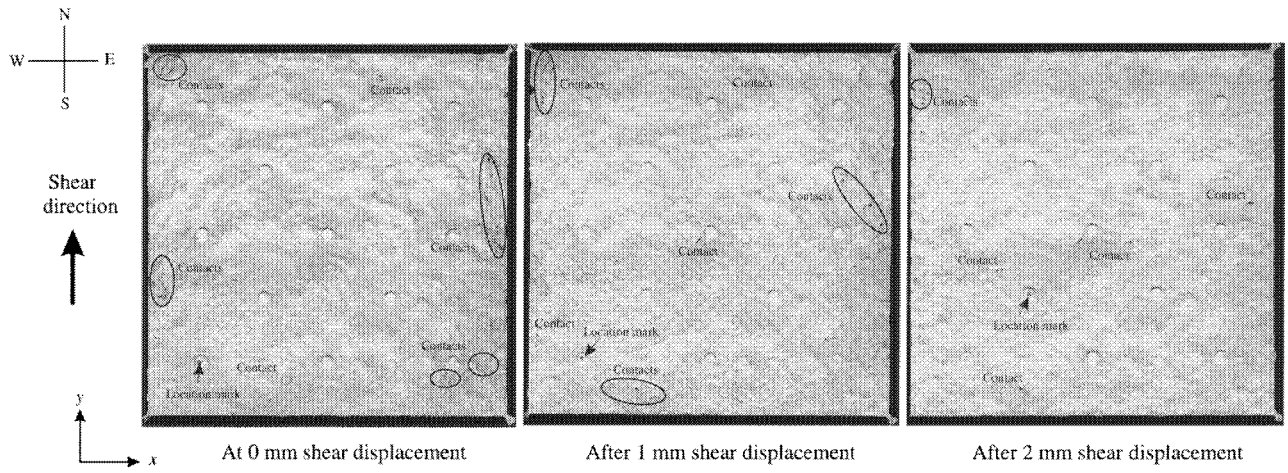

Fig. 5. Aperture replicas showing void geometry of a rock fracture under different shear displacements. Lighter regions correspond to larger aperture; contact regions are indicated by the small black spots.

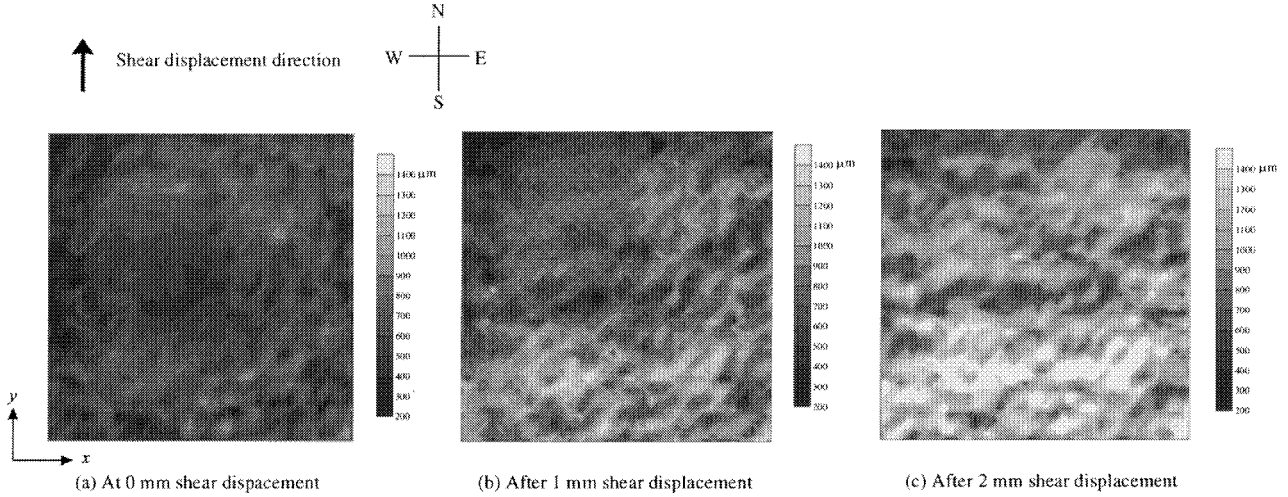

Fig. 6. Distributions of apertures measured at different shear displacements.

dotted horizontal line in Fig. 9), it was used as a sill to model the semivariograms. The semivariogram for the omnidirectional case can be fitted by a spherical model with a sill of 82500 μm^2 and a range of 16 mm. In the x and y directions, the semivariogram can be well-described by a spherical model, with a 92400 μm^2 sill and 24 mm range and by a spherical model with a 97900 μm^2 sill and 12 mm range, respectively. These different values of range show that the aperture is much more closely correlated in the x direction than in the y direction, which is confirmed by Figs 5 and 6 where the apertures can be seen aligned in the x direction at 2 mm shear displacement.

Table 2. Statistics of apertures measured at 0, 1 and 2 mm shear displacement using microscope

Shear displacement	0 mm	1 mm	2 mm
No. of data	1600	1600	1600
Mean, $\langle e \rangle$ (μm)	607	712	1024
Standard deviation, s (μm)	160	221	332
$s/\langle e \rangle$	0.26	0.31	0.32
Maximum aperture (μm)	1217	1496	2083
Minimum aperture (μm)	59	53	84

At zero shear displacement, semivariograms are not clearly distinguished from one another in either the omnidirection or in the x and y directions, indicating that the fracture has a similar spatial correlation structure in all directions. As shear displacement increases, semivariograms in the x direction lie lower compared with the variance of apertures than those in the y direction, suggesting that the aperture distribution become more closely correlated in the x direction than in the y direction, with increasing shear displacement.

NUMERICAL MODELLING

Governing equation

Under certain geometric and kinematic conditions, namely that flowrate is low and the aperture does not vary too abruptly, the simpler Reynolds lubrication equation can be used to describe steady flow in fractures [13], rather than the full Navier–Stokes

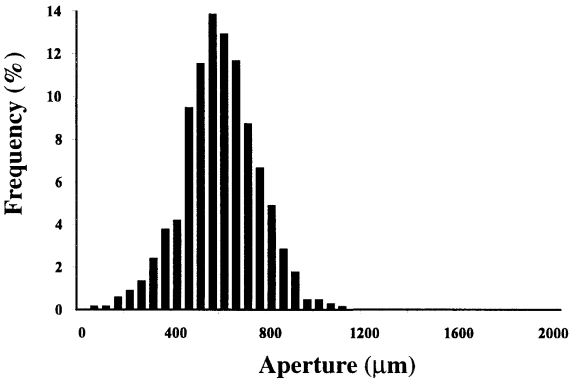

(a) At 0 mm shear displacement

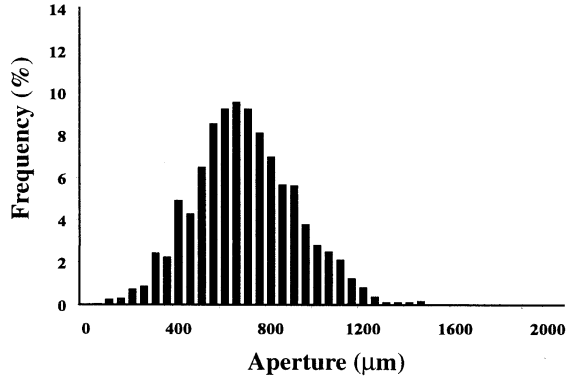

(b) After 1 mm shear displacement

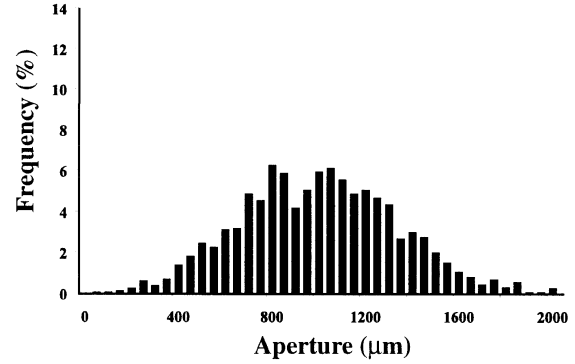

(c) After 2 mm shear displacement

Fig. 7. Frequency histograms of apertures measured at different shear displacements.

equations. The Reynolds equation is

$$\frac{\partial}{\partial x}\left(\frac{\rho g e^3(x,y)}{12\mu}\frac{\partial h}{\partial x}\right)+\frac{\partial}{\partial y}\left(\frac{\rho g e^3(x,y)}{12\mu}\frac{\partial h}{\partial y}\right)+Q=0, \tag{2}$$

where Q is an internal source or sink (for example, to represent fluid withdrawal by pumping or injection), taken to be positive if fluid is flowing into the rock fracture and negative if flowing out of the rock fracture, g is the gravitational acceleration, e is aperture, ρ is the density of the fluid and μ is the dynamic viscosity of the fluid.

The weighted residual method, in particular Galerkin's method, is applied to derive the governing equation [34, 35] from the Reynolds equation:

$$\left(\int\int_{S^{(m)}}[B^{(m)}]^{\mathrm{T}}[D^{(m)}][B^{(m)}]\,\mathrm{d}S\right)\{H^{(m)}\} - \left[\int_{L^{(m)}}[N^{(m)}]^{\mathrm{T}}\left(\frac{\rho g e^{(m)3}}{12\mu}\frac{\partial h}{\partial x}l_x+\frac{\rho g e^{(m)3}}{12\mu}\frac{\partial h}{\partial y}l_y\right)\mathrm{d}L + \int\int_{S^{(m)}}Q^{(m)}[N^{(m)}]^{\mathrm{T}}\,\mathrm{d}S\right]=0, \tag{3}$$

where $[N^{(m)}]$ is the row vector containing the interpolation functions in the element m, $S^{(m)}$ is a surface of the element, $L^{(m)}$ is a boundary of the region under consideration, $\{H^{(m)}\}$ is the hydraulic head matrix and l_x and l_x are the x and y direction cosines of the normal to the boundary, respectively. If zero flow is specified, or if the boundary is impermeable, the first term in the square brackets will be zero. The second term in the square brackets represents the flowrates at nodes located at those points with known flowrates, called Neumann nodes. The elements of the $[B]$ matrix are defined as

$$\left\{\begin{array}{c}\dfrac{\partial h}{\partial x}\\[2ex]\dfrac{\partial h}{\partial y}\end{array}\right\}=\left\{\begin{array}{c}\dfrac{\partial[N^{(m)}]^{\mathrm{T}}}{\partial x}\\[2ex]\dfrac{\partial[N^{(m)}]^{\mathrm{T}}}{\partial y}\end{array}\right\}\{H^{(m)}\}=[B^{(m)}]\{H^{(m)}\}. \tag{4}$$

The hydraulic transmissivity matrix is given by

$$[D^{(m)}]=\left[\begin{array}{cc}\dfrac{\rho g e^{(m)3}}{12\mu} & 0\\[2ex] 0 & \dfrac{\rho g e^{(m)3}}{12\mu}\end{array}\right]. \tag{5}$$

Equation (3) can be rewritten as

$$[K^{(m)}]\{H^{(m)}\}-\{F^{(m)}\}=0, \tag{6}$$

where $[K^{(m)}]$ is the conductance matrix. For the whole region, Equation (6) becomes

$$\sum_{m=1}^{N}([K^{(m)}]\{H^{(m)}\}-\{F^{(m)}\})=0. \tag{7}$$

The finite element code ROCKFLOW was written in the C language to solve the above equations. It is based on the code GW1, developed by Istok [36] to solve the mathematically analogous equations of groundwater flow in an inhomogeneous aquifer. Linear quadrilateral, quadratic quadrilateral and linear triangle elements were adopted as element shapes. All elements are isoparametric, for which the order of the hydraulic head interpolation function and the geometry shape function should be the same. The density, the dynamic viscosity of water, and the gravitational

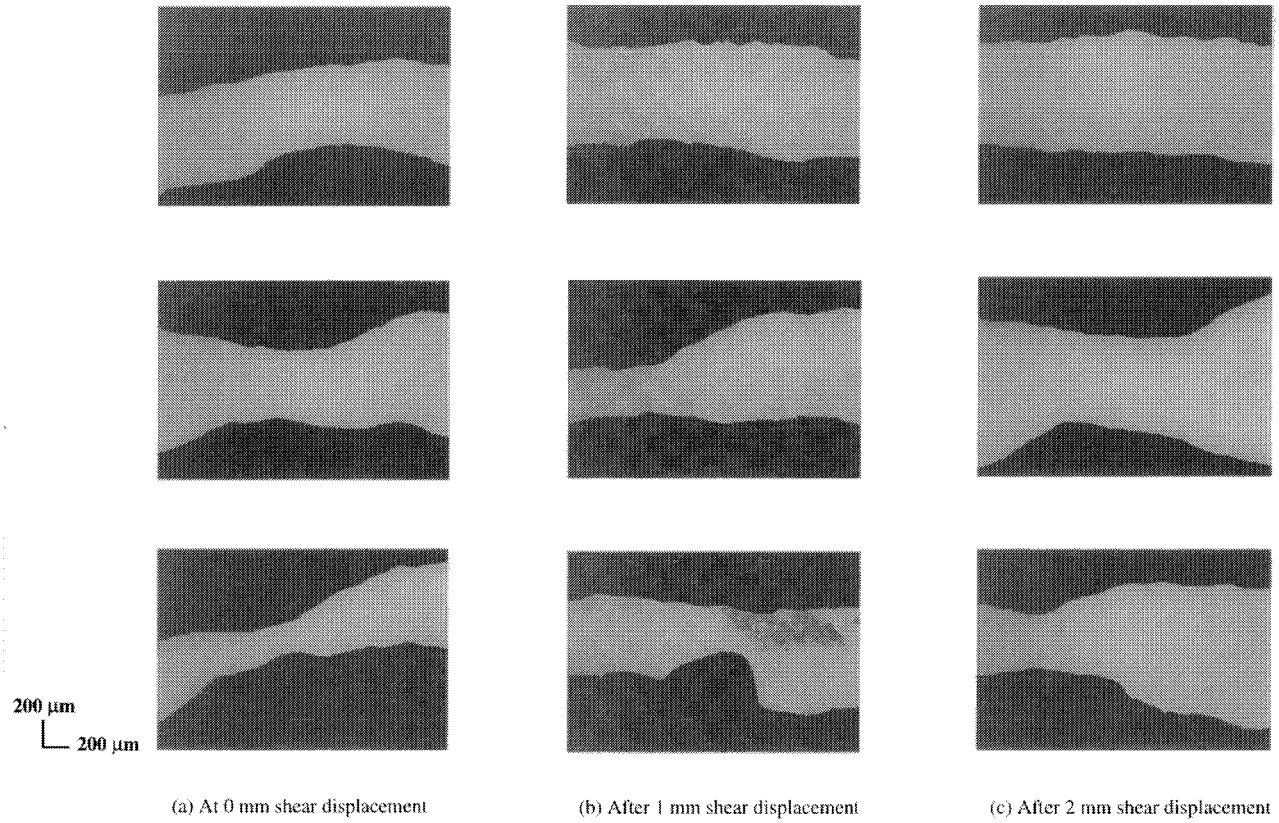

Fig. 8. Examples of aperture profiles along the x direction at 0, 1 and 2 mm shear displacements.

acceleration were taken as 1.00×10^3 kg/m^3, 1.00×10^{-3} Pa·s and 9.807 m/s^2, respectively [36]. ROCKFLOW calculates the hydraulic heads at all nodes and the velocity components at the centre of each element.

The code was verified by simulating flow through arrays of elements arranged such that the aperture varied either in the direction of flow, or in the direction transverse to flow. In these cases the hydraulic aperture is given (exactly) by the cube root of the harmonic or arithmetic means of e^3, respectively, i.e.

$$e_h(\text{series}) = \langle e^{-3} \rangle^{-1/3}, \qquad e_h(\text{parallel}) = \langle e^3 \rangle^{1/3}. \quad (8)$$

The numerical simulations using ROCKFLOW led to hydraulic apertures that agreed with these two theoretical series and parallel results to within better than 0.1%. The code was also verified in other simple cases for which the exact result is known, such as flow around a circular obstacle. In all such cases, ROCKFLOW gave errors of less than 1%, as long as a sufficiently fine grid was used; see Ref. [27] for more details.

METHODOLOGY TO ANALYSE FLOW TEST RESULTS

Hydraulic heads were measured over the fracture during radial and unidirectional flow tests. Although constant hydraulic head was maintained in the water container that fed into the central hole and at the outer boundaries of the fracture, measured heads in the fracture were much lower than the overall imposed head drop, indicating that most of head loss took place outside the fracture, not in the fracture, even though the hydraulic supply had been designed to avoid this as far as possible. It is thought that substantial head losses took place in the tubes and especially the connectors [37], before entering the fracture and after exiting the fracture (Fig. 3). This was verified by performing flow tests without having a fracture in place, to investigate the hydraulic properties of the apparatus itself (see Ref. [27] for details).

In the case of radial flow tests, heads on two concentric circles could be measured and averaged [see Fig. 10(a)], so as to calculate the hydraulic aperture and actual head drop within the fracture. The Thiem equation [38] was used to calculate the hydraulic aperture using the measured heads on the two concentric circles:

$$e_h^3 = \frac{12\mu \ln(r_o/r_i) Q_0}{2\pi\rho g \Delta h}, \quad (9)$$

where r_o is the radius of the outer circle and r_i is the radius of the inner circle. (In radial flow tests, it is not entirely proper to take the average of the heads, because hydraulic heads in the northern parts on two concentric circles are quite different from those in the southern parts, especially at 1 and 2 mm shear displacements; however, we note that the hydraulic aperture measured from the radial flow tests using this method is consistent with that of the unidirectional flow tests.)

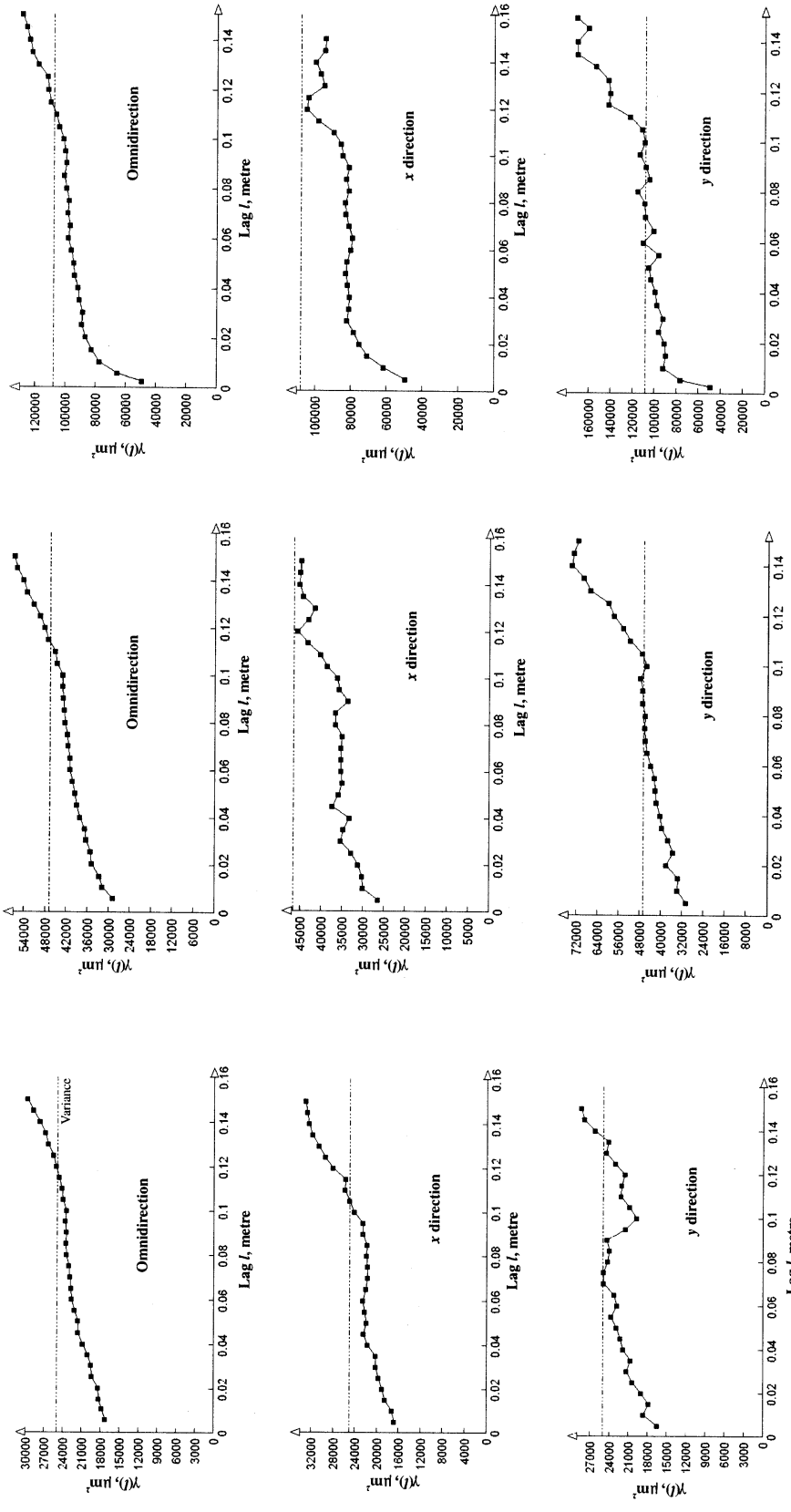

(a) At 0 mm shear displacement (b) After 1 mm shear displacement (c) After 2 mm shear displacement

Fig. 9. Semivariograms for spatial correlation of apertures. Dotted horizontal line represents the variance of the apertures.

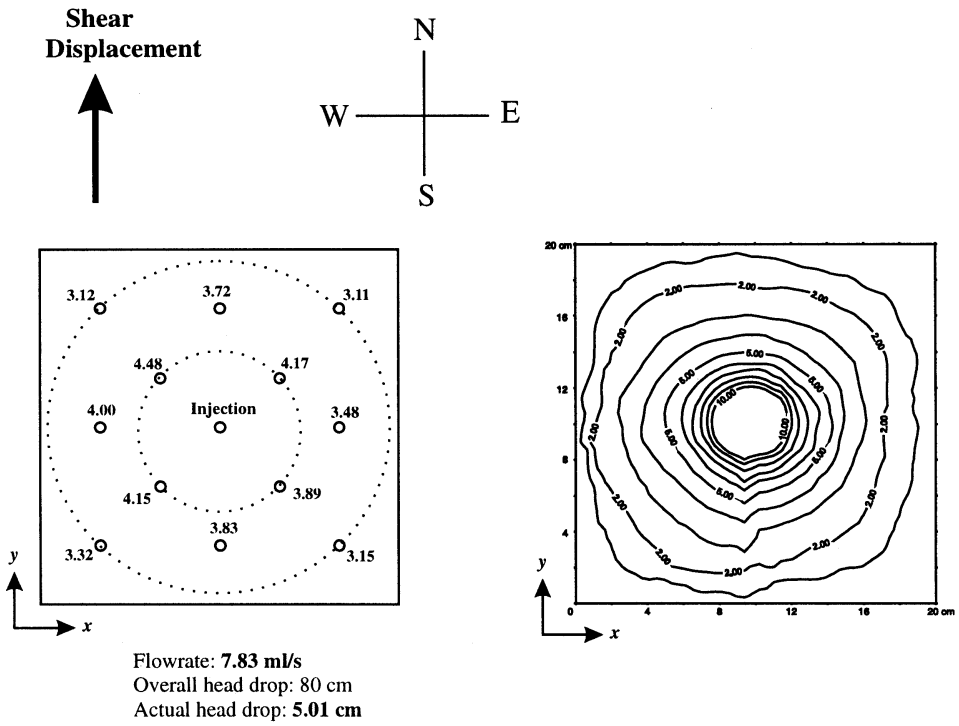

(a) Radial flow test at overall head drop of 80 cm

(b) Radial flow simulation

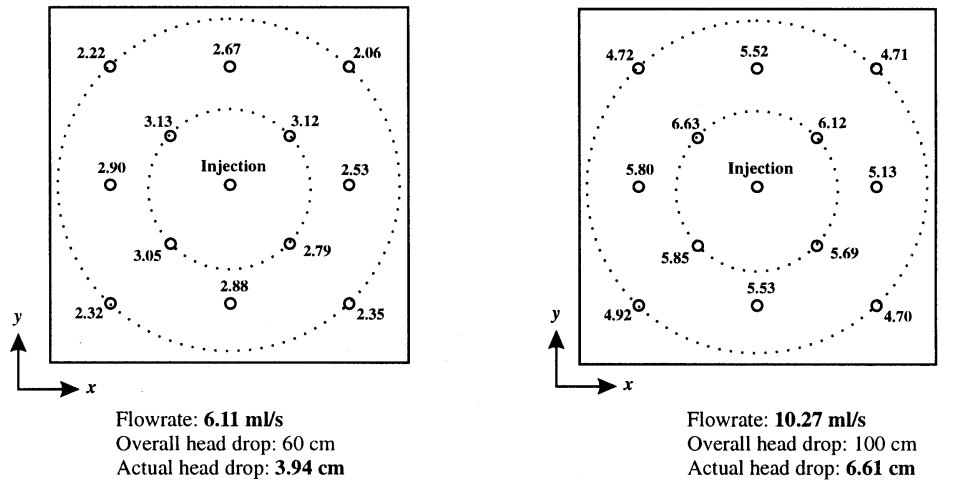

(c) Radial flow test at overall head drop of 60 cm

(d) Radial flow test at overall head drop of 100 cm

Fig. 10. Hydraulic heads measured from radial flow tests at different overall head drops, and head distribution calculated by numerical simulation at zero shear displacement. Actual head drops are calculated between the injection hole and the outer circle.

As head losses also took place outside the fracture during unidirectional flow, the actual head drop for these cases was also calculated by taking the average heads measured between two lines in the x and y direction for the x- and y-directional flow, respectively, as shown later by the dotted lines in Fig. 12. Considering the inner area between two straight lines of measurements, the hydraulic apertures for flow in the x and y directions were calculated with the aid of the cubic law and the actual head drop.

HYDRAULIC PROPERTIES AFTER SHEAR DISPLACEMENT

At zero shear displacement

The results of radial flow tests are shown in Fig. 10(a). Although 80 cm of head difference was applied to the overall experimental apparatus, the actual hydraulic head drop occurring in the fracture was much less, due to losses in the tubing and connectors. The Thiem equation was used to calculate the

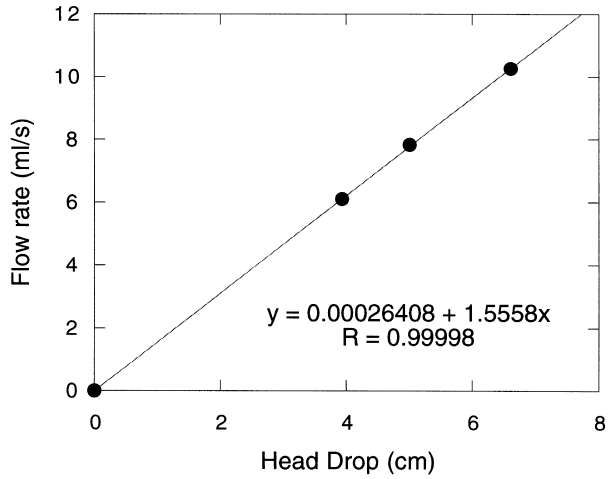

Fig. 11. Relation between actual head drop and flowrate measured from radial flow tests at zero shear displacement.

hydraulic aperture as explained above and the hydraulic aperture was found to be 474 μm.

The hydraulic heads measured at the monitoring holes along the inner circle show great variability, despite being at the same distance from the injection hole, indicating that the fracture is hydraulically inhomogeneous at this scale. The hydraulic heads measured on the outer circle are generally similar to one another, showing that the fracture becomes homogeneous and isotropic with increasing scale. Radial flow having 30 cm of head drop was numerically simulated using the ROCKFLOW code and the measured apertures. The hydraulic head distribution predicted by this simulation is shown in Fig. 10(b) and this flow pattern shows a macroscopically isotropic medium and qualitative agreement between the shapes of the isopotential curves. Note that the overall head drop used in the numerical simulation was different from that which occurred in the actual flow tests, so the comparison between Fig. 10(a) and (b) can only be qualitative.

Radial flow tests were conducted at two different overall head drops: 60 and 100 cm (Fig. 10). Again, in order to eliminate the effect of head losses in the tubing and connectors, the hydraulic heads on two concentric circles were used to calculate the hydraulic aperture and actual head drop in the fracture between the injection and the outer circle. The hydraulic aperture was calculated as 473 μm for both cases. The patterns of measured head distributions agreed with that estimated at 80 cm of overall head drop (Fig. 10). In Fig. 11, actual flowrates are plotted against actual head drops occurring between the injection hole and the outer circle in the fracture. The line connecting the three points goes through the origin and the relation shows linear laminar flow. The Reynolds number, Re, was calculated by

$$\mathrm{Re} = \frac{2\rho\bar{u}e}{\mu}, \tag{10}$$

where $\bar{u}$ is the velocity and e is the hydraulic aperture. The Reynolds number was calculated as 25, based on the results of 5.01 cm of actual head drop (80 cm of overall head drop). This Reynolds number is much smaller than the critical Reynolds number that determines the onset of non-linear flow, which can be estimated from the chart constructed by Louis [37]. For

Table 3. Comparison of hydraulic apertures obtained from experiment with numerical and theoretical estimates. All hydraulic apertures of radial flow tests were based on 80 cm of overall head drop

Shear	Approach	Flow type	Hydraulic aperture
0 mm displacement	experimental	radial	474 μm
		x-directional	469 μm
		y-directional	446 μm
		anisotropy ratio η	0.86
	numerical	radial	530 μm
		x-directional	586 μm
		y-directional	599 μm
		anisotropy ratio η	1.02
1 mm displacement	experimental	radial	629 μm
		x-directional	664 μm
		y-directional	577 μm
		anisotropy ratio η	0.66
	numerical	radial	667 μm
		x-directional	723 μm
		y-directional	665 μm
		anisotropy ratio η	0.78
2 mm displacement	experimental	radial	753 μm
		x-directional	852 μm
		y-directional	740 μm
		anisotropy ratio η	0.66
	numerical	radial	1007 μm
		x-directional	1058 μm
		y-directional	925 μm
		anisotropy ratio η	0.67

fractures having a ratio of standard deviation to mean aperture of about 0.3, such as observed in our tests, Louis' chart yields a critical Reynolds number of about 1000. This is consistent with our results showing a linear relationship between the head drop and the flowrate.

Hydraulic aperture obtained from the radial flow test was compared with numerical estimates (Table 3). Numerical simulation predicted a hydraulic aperture of 530 μm, which is 11% higher than the experimental hydraulic aperture of 474 μm.

Unidirectional flow tests were conducted along the x and y directions, with 30 cm of head drop applied between the inlet and outlet boundaries of the system (Fig. 12). Again, most of the head drop occurred within the tubing and connectors, so the average head drop within the fracture itself was calculated from the averages of three readings taken along each of the dotted lines shown in Fig. 12. Actual head drops in the x- and y-directional flows were 4.16 and 3.49 cm in the inner area between the two dotted lines, respectively. The hydraulic apertures in the x and y directions were calculated as 469 and 446 μm with the aid of the cubic law, yielding an anisotropy ratio of 0.86 (Table 3). The Reynolds numbers were 50 and 36 in the x- and y-directional flow. The hydraulic apertures obtained from unidirectional flow tests are consistent with those found from the radial flow tests. In the x- and y-directional flow simulations, the hydraulic apertures were 586 and 599 μm, respectively, yielding an anisotropy ratio of 1.02 (Table 3). The hydraulic apertures measured by the x- and y-directional flow tests are 20 and 26% lower than the numerical estimates, respectively.

After 1 mm shear displacement

After 1 mm shear displacement, radial flow tests were conducted at 60 and 80 cm of overall head drop [Fig. 13(a)]. The hydraulic apertures were calculated as 636 and 629 μm, respectively, using the heads on the two concentric circles and the Thiem equation; the actual head drops between the injection well and the

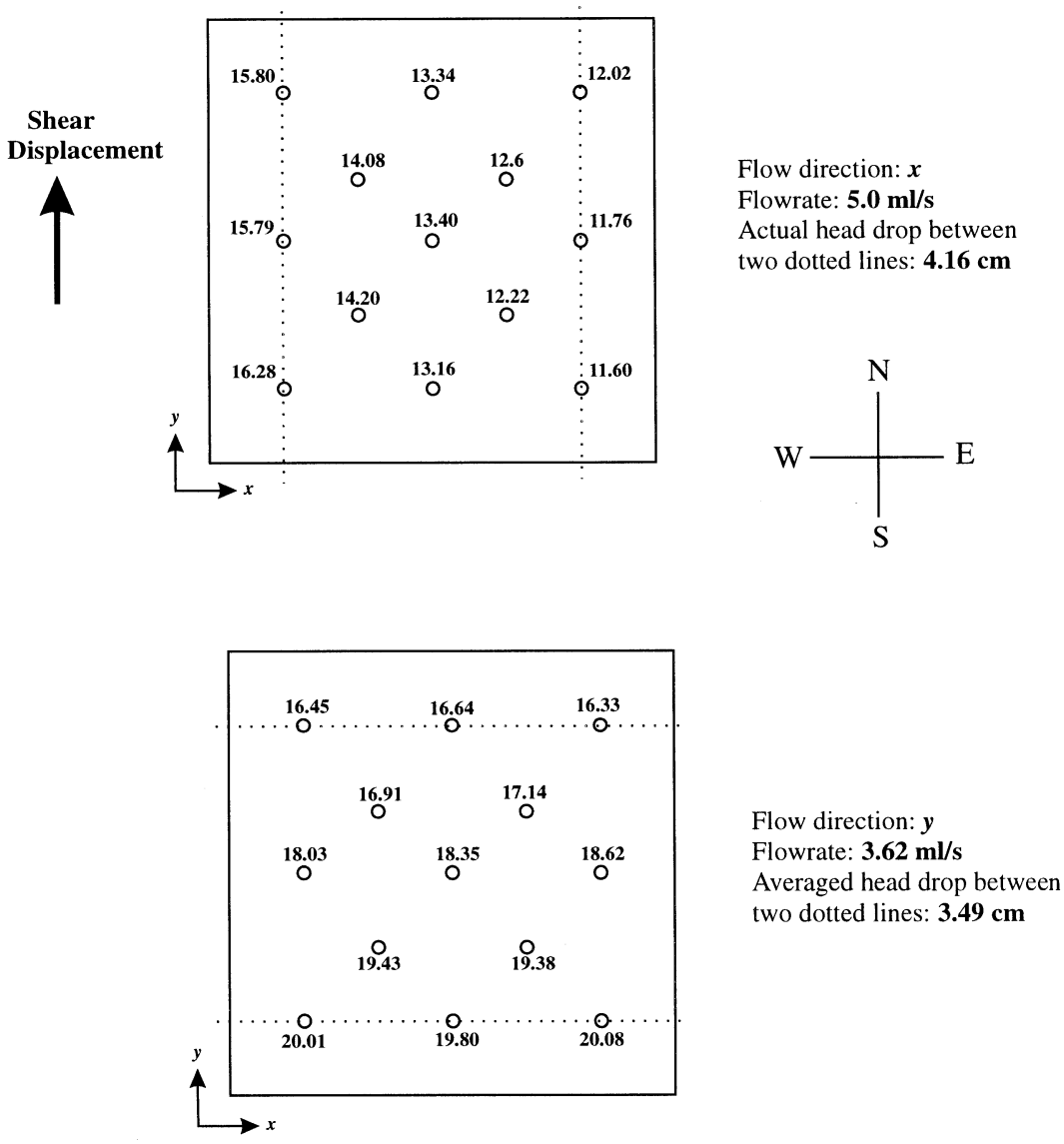

Fig. 12. Hydraulic heads and flowrate measured during unidirectional flow tests at zero shear displacement.

outer circle were calculated as 3.33 and 3.99 cm, respectively. The northern part of the fracture is more transmissive than the southern part, indicating that the fracture is inhomogeneous in the y direction. The valley having smaller apertures just south of the injection hole and trending in the x direction contributes to much head loss in the southern part [Fig. 5 and Fig. 6(b)]. On the other hand, the valley at the northern edge and trending in the x direction is located outside the monitoring holes and does not affect the measured hydraulic heads. When compared in the east–west direction, the measured heads are similar at monitoring holes located at the same distance from the injection hole, as expected from Fig. 5and Fig. 6(b).

Radial flow simulations were conducted under 30 cm of head drop using the measured apertures [Fig. 13(b)]. The hydraulic head distribution obtained from radial simulation shows that much head loss takes place in the region just south of the injection hole, and in the northern area along the x direction. The radial flow simulation yielded hydraulic apertures of 667 μm, showing 6% discrepancy with the experimental value (Table 3).

The Reynolds number was calculated as 47 at 80 cm of overall head drop, which is much smaller than the critical Reynolds number 1000 suggested by Louis. Hakami [28] reported that the relation between flowrate and head drop was linear for Reynolds numbers in the range of 40–73 (estimated by the authors for the flow tests reported by Hakami [28] at 0.4 MPa normal load with 1 to 2.2 m head drops). In addition, radial flow at zero shear displacement indicated a linear flow regime, although the Reynolds number was 25.

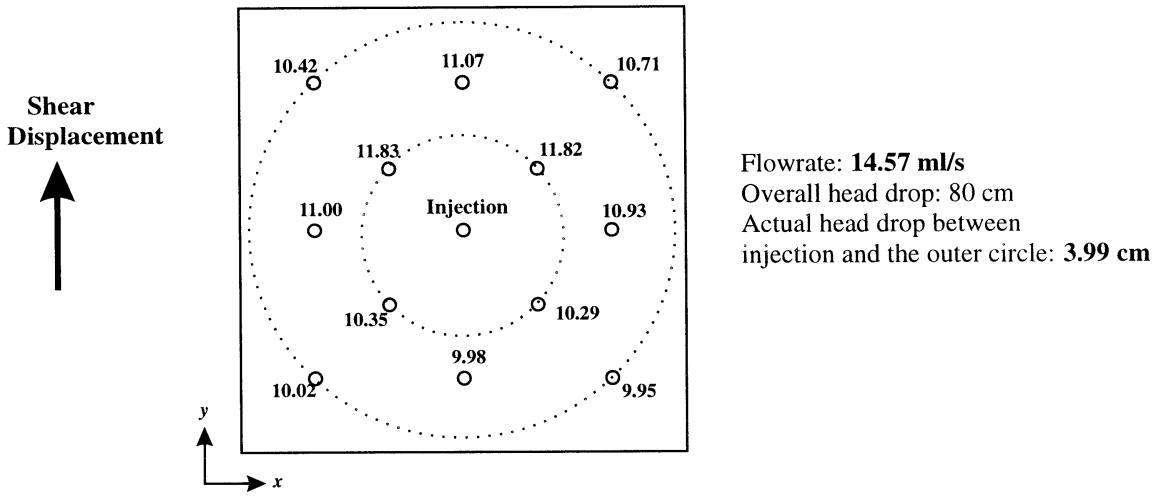

(a) Radial flow test

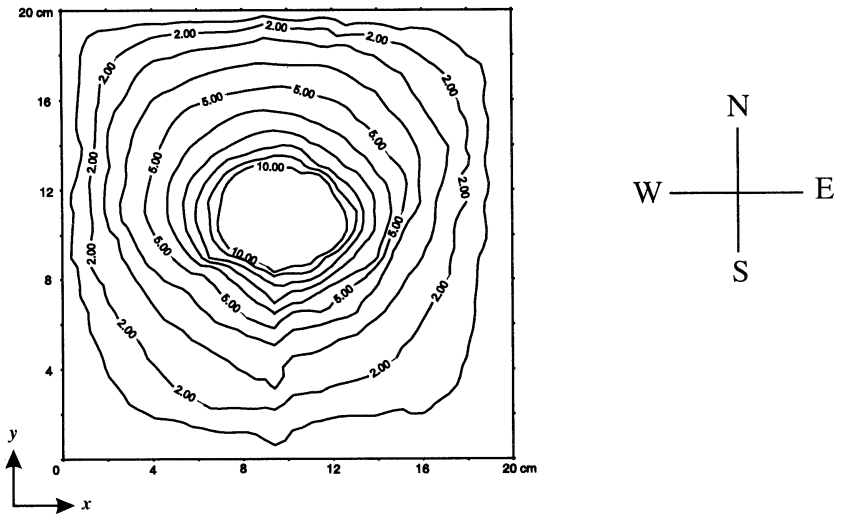

(b) Radial flow simulation

Fig. 13. Hydraulic heads measured from radial flow test, and head distribution calculated by numerical simulation at 1 mm shear displacement.

Unidirectional flow tests were conducted along the x and y directions. Although 30 cm of head drop was applied at the entrance and exit boundaries, the actual head drops which took place between two dotted lines in the x- and y-directional flow tests were 1.697 and 0.803 cm, respectively (Fig. 14). These are much lower than in the case of zero shear displacement, because the increase in aperture results in less resistance. With the aid of the cubic law and the average actual head drop, the hydraulic apertures of the x and y directions were calculated as 664 and 577 μm, which yields an anisotropy ratio 0.66. As mentioned before, the valleys having smaller apertures along the x direction made a contribution to the anisotropic behaviour. The Reynolds numbers were found to be 58 and 18 in the x- and y-directional flow, respectively.

In numerical simulations, the hydraulic apertures in the x and y directions were 723 and 665 μm, respectively, leading to an anisotropy ratio of 0.78 (Table 3). The hydraulic apertures measured by unidirectional flow tests are 8% lower than the numerical estimates in the x-direction and 13% lower in the y-direction. Although a slight discrepancy exists between measured and predicted anisotropy ratios, both values show that the fracture is more permeable in the x direction than in the y direction.

After 2 mm shear displacement

At this shear displacement, radial flow tests were conducted only at 80 cm and 100 cm of overall head drop, because the head drops within the fracture itself were too small to measure when the overall head drop was less than 80 cm. For the 80 and 100 cm head drop cases, the hydraulic apertures were calculated as 753 and 730 μm, respectively, using the heads on two concentric circles and the Thiem equation. The hydraulic aperture increases with increasing shear displacement, as expected, but the increase of the hydraulic aperture from 1 and 2 mm shear displacements is relatively small compared with the sharp increase in the mean aperture (Table 3).

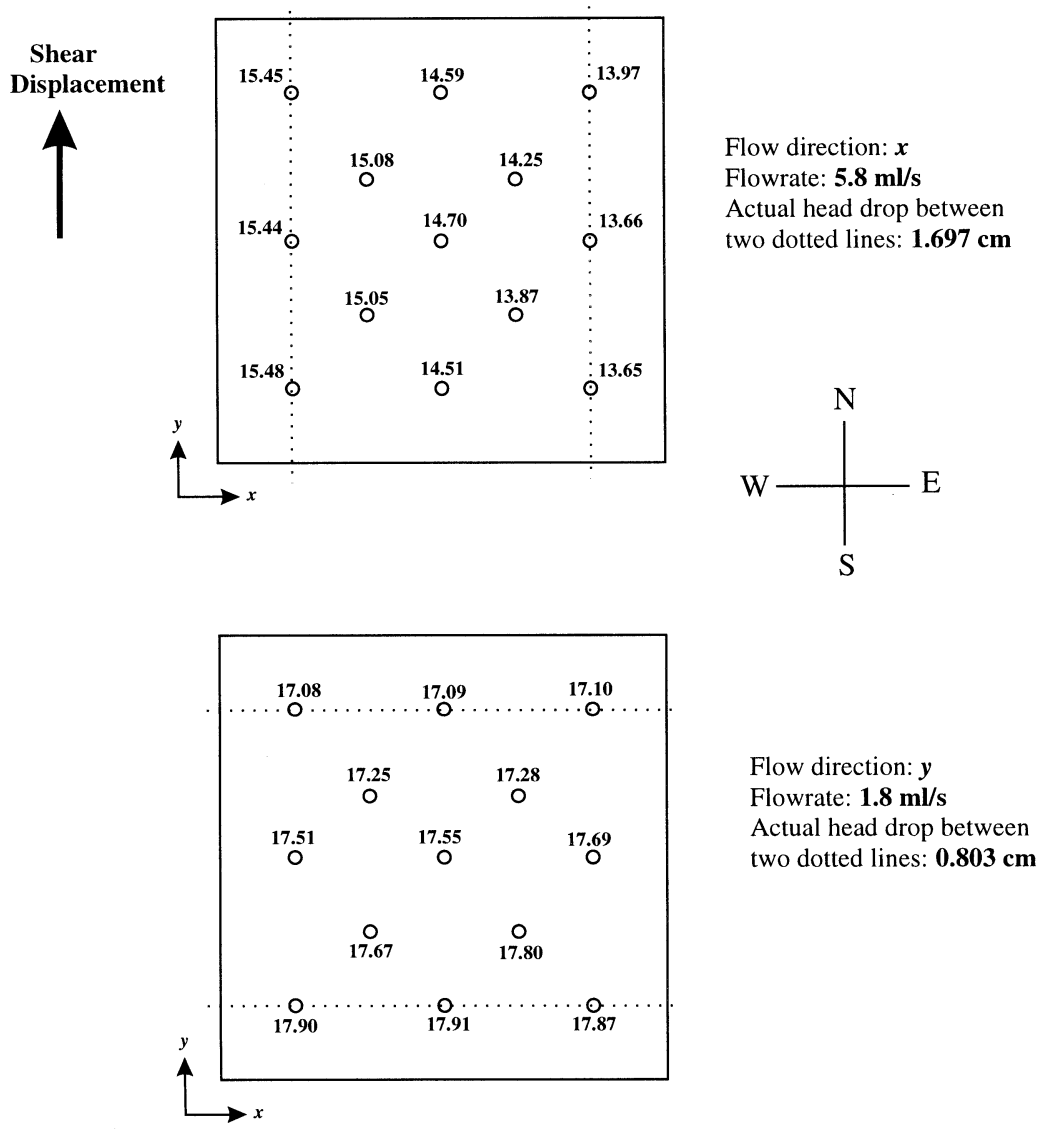

Fig. 14. Hydraulic heads and flowrate measured during unidirectional flow tests at 1 mm shear displacement.

Figure 15(a) shows the measured hydraulic head, and the actual head drop of 2.01 cm calculated by the Thiem equation between the injection point and the outer concentric circle, for the case of 80 cm overall head drop. Measured hydraulic heads indicate that the fracture is inhomogeneous in the y direction parallel to shear displacement, because of the smaller aperture valley located just south of the injection hole (Figs 5 and 6), but the fracture is almost hydraulically homogeneous in the x direction, as indicated by comparing the heads in the east–west directions [see also Fig. 5 and Fig. 6(c)].

The hydraulic head distribution was obtained from radial flow simulation under 30 cm of head drop [Fig. 15(b)]. The hydraulic head decreases sharply in the regions located just south of the injection hole and at the northern edge along the x direction, in the area of smaller aperture valleys; this corresponds to the flow pattern observed in the flow tests. The radial flow simulation predicted the hydraulic aperture 1007 μm (Table 3), showing about 25% disagreement with the hydraulic aperture measured by radial flow tests.

The Reynolds number was calculated to be 40 at 80 cm of overall head drop, which is in the linear flow regime according to Louis' critical Reynolds number of 1000 and according to Hakami's experimental findings [28].

The overall head drop in unidirectional flow tests was 30 cm, but the actual head drops which took place between two dotted lines in the x- and y-directional flow tests were only 0.83 and 0.704 cm, respectively (Fig. 16). Based on this head drop, the hydraulic apertures in the x and y directions were found to be 852 and 740 μm, yielding an anisotropy

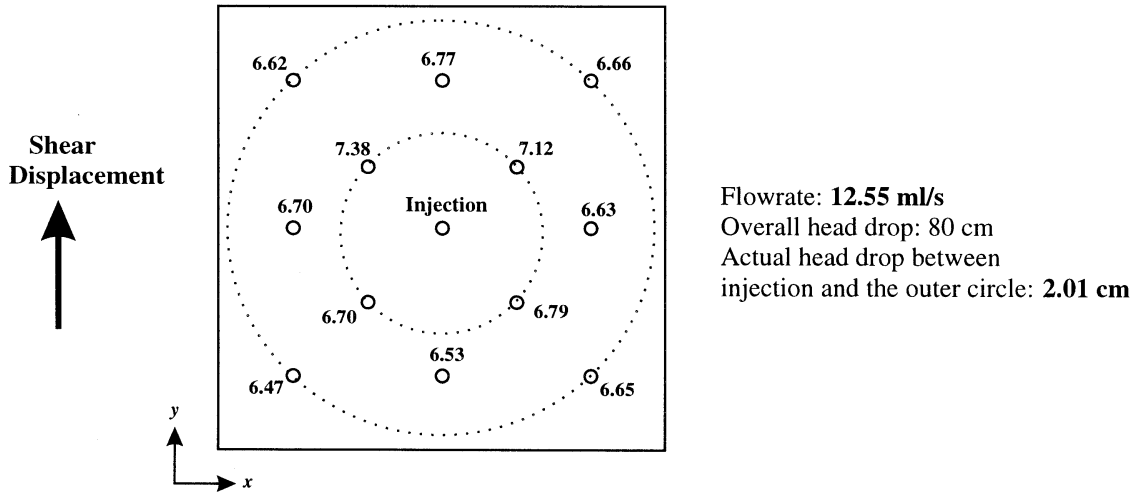

(a) Radial flow test

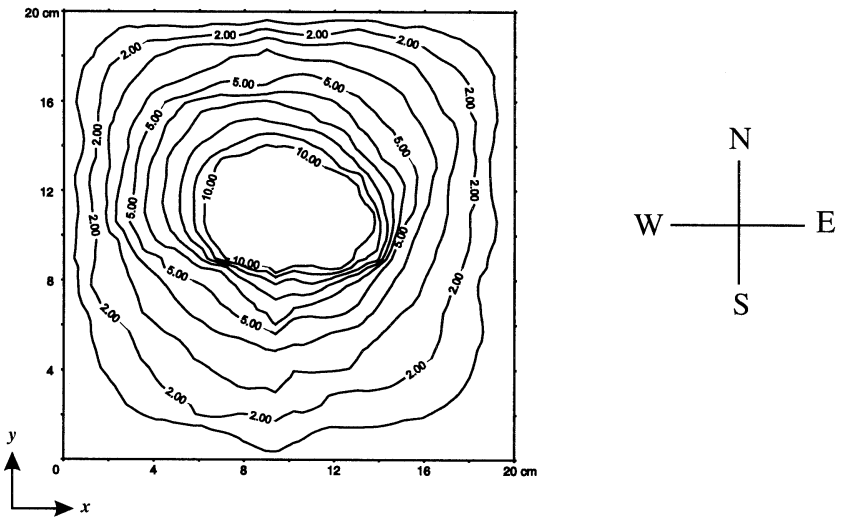

(b) Radial flow simulation

Fig. 15. Hydraulic heads measured from radial flow test, and head distribution calculated by numerical simulation at 2 mm shear displacement.

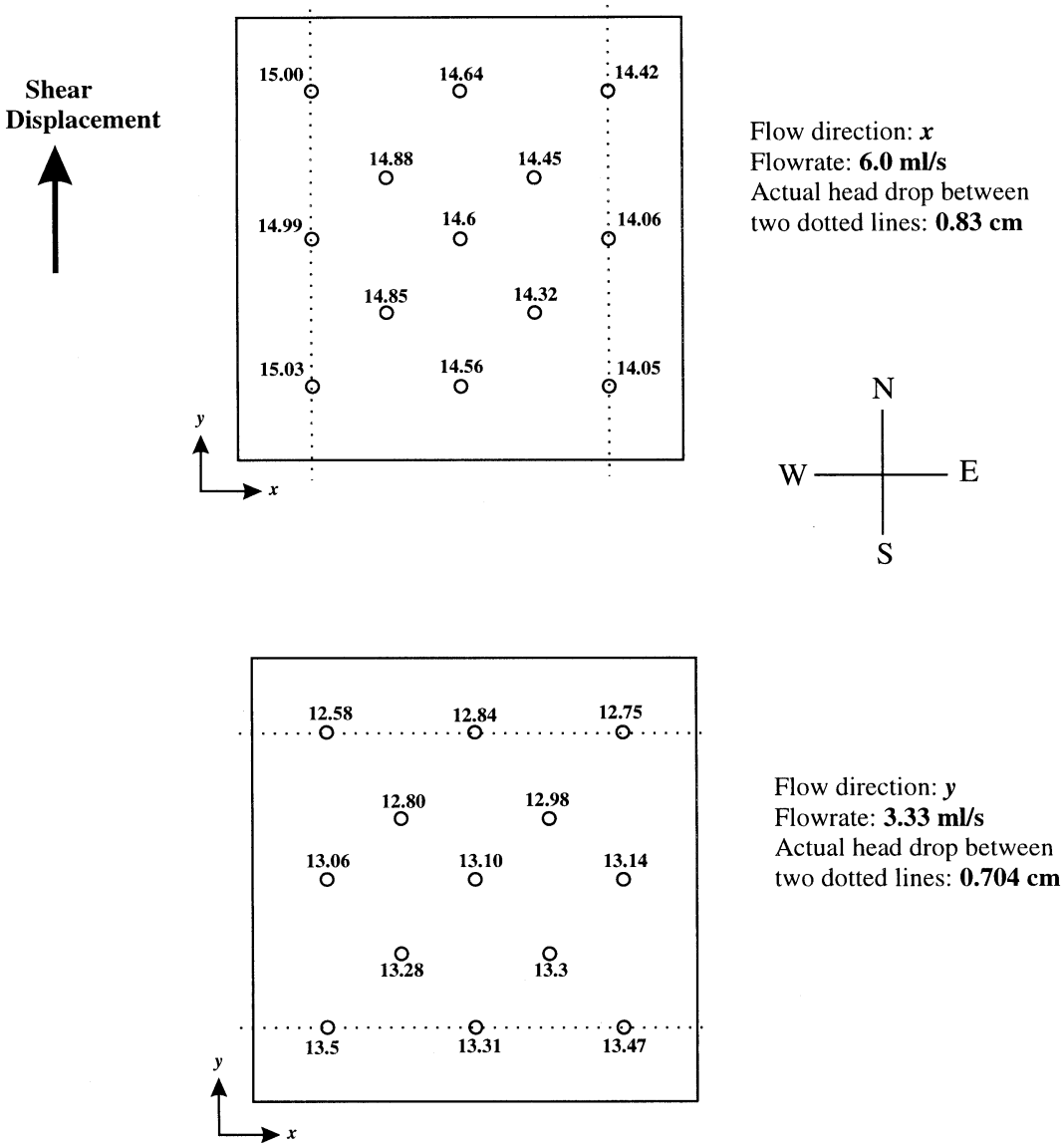

Fig. 16. Hydraulic heads and flowrate measured during unidirectional flow tests at 2 mm shear displacement.

ratio of 0.66. The smaller aperture valleys aligned along the x direction block the flow in the y direction, resulting in the anisotropic hydraulic properties. The Reynolds numbers were 60 and 33 in the x- and y-directional flow tests.

The numerical simulations gave hydraulic apertures in the x and y directions of 1058 and 925 μm, respectively, leading to an anisotropy ratio of 0.67 (Table 3). The hydraulic apertures measured by unidirectional flow tests are 19 and 20% lower than these numerical estimates, respectively. Although discrepancies exist between measured and predicted hydraulic aperture, the anisotropy ratios agree with each other, indicating that the fracture is more permeable in the x direction than in the y direction. Flow tests and numerical simulations show that with increasing shear displacement, the hydraulic aperture increases and the fracture becomes more hydraulically anisotropic.

VALIDITY OF REYNOLDS EQUATION

Numerical simulations yielded a discrepancy of 20–25% with the hydraulic apertures measured in the radial and unidirectional flow tests, except in the case of 1 mm shear displacement, where the difference was about 10%. Two possible explanations for this discrepancy suggest themselves: inertial effect due to high Reynolds number, or the discrepancy between the Reynolds equation and the Navier–Stokes equations caused by geometrical characteristics such as abrupt changes in the aperture. Throughout all flow tests, the Reynolds numbers of 18–60 were much lower than the value of about 1000 suggested by Louis [37] at which inertial effects begin to cause nonlinearities in the relationship between head drop and flowrate. The radial flow tests at zero shear displacement showed a linear relation between flowrate and head drop, and Hakami's experimental results [28] showed that linear

flow was observed for Reynolds numbers in the range of 40 to 73. This evidence seems to rule out inertial effects as the cause of the discrepancy.

In an attempt to explain the discrepancy between numerical estimates and measured hydraulic apertures, the following equation suggested by Hasegawa and Izuchi [39, 40] was used:

$$e_h = e_R\left[1 - \frac{3\pi^2(1-\delta^2)\delta^4}{5(1+\delta^2/2)}\left(1+\frac{13}{8085}\mathrm{Re}^2\right)\frac{\langle e\rangle^2}{\Lambda^2}\right]^{1/3}, \quad (11)$$

where e_R is hydraulic aperture predicted by the Reynolds equation, δ is defined as $\sqrt{2}s/\langle e\rangle$ and Λ is the spatial wavelength of the aperture. Equation (11) is a perturbation solution, exact to second-order in Re and $\langle e\rangle/\Lambda$, for flow through a sinusoidal channel. Although this idealised geometry is not quite the same as the actual geometry of our rough-walled fractures, Equation (11) is the only analytical solution we are aware of that allows a quantitative estimation of the errors incurred by using the Reynolds equation, for a geometry that in some way resembles that of a rock fracture. The second term in the square bracket represents the discrepancy between the predictions of the Navier–Stokes equations and the Reynolds equation. The parameter δ can be estimated from aperture data. Although the aperture varies very gradually over distances 2.5 times greater than the mean aperture (i.e. $\Lambda > 2.5\langle e\rangle$), the geometrical parameter $\langle e\rangle/\Lambda$ was taken to be 0.4, for the worst case, based on our 1600 microscope measurements of the real aperture. Inserting δ, $\langle e\rangle/\Lambda$ and Re in Equation (11) leads to an estimate of the maximum discrepancy due to the combined effects of Reynolds number and rapid aperture variations.

In the case of the x-directional flow test at 2 mm shear displacement, the hydraulic aperture 852 μm was 19% lower than the numerical estimate of 1058 μm (Table 3). The terms $\langle e\rangle/\Lambda = 0.4$, $\delta = 0.45$, and $\mathrm{Re} = 60$ were inserted into the square brackets of Equation (11) in an attempt to explain this discrepancy. The correction term yielded 0.932; i.e. a maximum 6.8% discrepancy can be attributed to the effects of Reynolds number and high spatial frequency. The numerical estimate of 1058 μm was thereby corrected to 986 μm, leaving a discrepancy of 13.6% yet unaccounted for. This may be because for $\mathrm{Re} > 1$, it may no longer be acceptable to ignore higher powers of the Reynolds number in the perturbation series solution to the Navier–Stokes equations, which were not found by Hasegawa and Izuchi. Hakami [28] also found that hydraulic apertures were 25% lower than the numerical estimates based on the Reynolds equation. Mourzenko *et al.* [41] found that the Reynolds equation predicted hydraulic apertures about 25% greater than the Stokes equation (which accounts for rapid aperture variations, but not for the inertial effects associated with high Reynolds numbers). However, Mourzenko *et al.* [41] did not use actual aperture data, only simulated data. Furthermore, they used a very coarse grid in their calculations. Hence, the question of why the Reynolds equation seems to slightly overpredict the hydraulic aperture remains open.

CONCLUSIONS

Aperture replicas were made on a natural sandstone fracture 0, 1 and 2 mm shear displacement. The mean aperture, calculated by weighing the aperture replica and using the density of Silcoset, showed very good agreement with that measured using a microscope. The aperture was measured from the fracture replica at 1600 known x and y co-ordinates for each shear condition, using a microscope. With increasing shear displacement, mean aperture and standard deviation increased, and the ratio of standard deviation to mean aperture increased slightly from 0.26 to 0.32. Frequency histograms were well-fitted by a normal distribution. Semivariograms analysis showed that as shear displacement increased in the direction normal to the roughness ridges which were aligned along the x direction, the apertures became more closely correlated to each other in the x direction rather than in the y direction.

Radial and unidirectional flow tests indicated that with increasing shear displacement, the fracture became heterogeneous and the anisotropy ratio decreased from 0.86 to 0.66, indicating that the fracture became more permeable in the x direction corresponding to the roughness ridges than in the y direction parallel to shear displacement. The hydraulic aperture observed during the radial flow experiments was in good agreement with the geometric mean of the two directional values measured in the uni-directional tests. Numerical simulations of flow using the Reynolds equation, along with the measured aperture field, showed about 10–25% discrepancy with the hydraulic apertures measured in the radial and unidirectional flow tests. The fact that the relationship between head drop and flowrate was linear in all of our experiments tends to refute the possibility that this is due to non-linear, high Reynolds number inertial effects. Furthermore, visual observation of the micrographs of the fracture aperture seem to show that the aperture varies sufficiently smoothly for the Reynolds equation to accurate approximate the Navier–Stokes equations [18]. Nevertheless, the discrepancy is too large to be explained as an artefact of experimental errors and so the cause of this discrepancy remains unresolved.

Acknowledgements—This work was supported by the Ministry of Education of the Republic of Korea, by a U.K. Overseas Research Students Award and by a grant from the Natural Environment Research Council, U.K. (Grant GR9/02289). This support is gratefully acknowledged.

Accepted for publication 28 May 1998

REFERENCES

1. Rouleau, A. and Gale, J. E., Statistical characterization of the fracture system in the Stripa granite, Sweden. *Int. J. Rock Mech. Min. Sci. Geomech. Abstr*., 1985, **22,** 353–367.
2. Pruess, K., Wang, J. S. Y. and Tsang, Y. W., On thermohydrologic conditions near high-level nuclear wastes emplaced in partially saturated fractured tuff. 1. Simulation studies with explicit consideration of fracture effects. *Water Resour. Res*., 1990, **26,** 1235–1248.
3. Neretnieks, I., Solute transport in fractured rock: Application to radionuclide waste repositories. In *Flow and Contaminant Transport in Fractured Rock*, eds. J. Bear, C.-F. Tsang and G. de Marsily. Academic Press, San Diego, 1993, pp. 39–127.
4. Rouleau, A. and Gale, J. E., Stochastic discrete fracture simulation of groundwater flow into an underground excavation in granite. *Int. J. Rock Mech. Min. Sci. Geomech. Abstr*., 1987, **24,** 99–112.
5. Pusch, R., Alteration of the hydraulic conductivity of rock by tunnel excavation. *Int. J. Rock Mech. Min. Sci. Geomech. Abstr*., 1989, **26,** 79–83.
6. Lindblom, U., The performance of water curtains surrounding rock caverns used for gas storage. *Int. J. Rock Mech. Min. Sci. Geomech. Abstr*., 1989, **26,** 85–97.
7. Lemos, J. V. and Lorig, L. J., Hydromechanical modelling of jointed rock masses using the distinct element method. In *Mech. of Jointed and Faulted Rock*, ed. H.-P. Rossmanith. Balkema, Rotterdam, 1990, pp. 605–611.
8. Kazemi, H. and Gilman, J. R., Multiphase flow in fractured petroleum reservoirs. In *Flow and Contaminant Transport in Fractured Rock*, eds. J. Bear, C.-F. Tsang and G. de Marsily. Academic Press, San Diego, 1993, pp. 267–323.
9. Smith, L. and Schwartz, F. W., Solute transport through fractured networks. In *Flow and Contaminant Transport in Fractured Rock*, eds. J. Bear, C.-F. Tsang and G. de Marsily. Academic Press, San Diego, 1993, pp. 129–167.
10. Witherspoon, P. A., Wang, J. S. Y., Iwai, K. and Gale, J. E., Validity of cubic law for fluid flow in a deformable rock fracture. *Water Resour. Res*., 1980, **16,** 1016–1024.
11. Tsang, Y. W., The effect of tortuosity of fluid flow through a single fracture. *Water Resour. Res*., 1984, **20,** 1209–1215.
12. Elliott, G. M., Brown, E. T., Boodt, P. I. and Hudson, J. A., Hydromechanical behaviour of joints in the Carnmenellis granite, S. W. England. In *Proc. Int. Symp. Fundamentals of Rock Joints*, ed. O. Stephansson. Balkema, Rotterdam, 1985, pp. 249–258.
13. Brown, S. R., Fluid flow through rock joints: the effect of surface roughness. *J. Geophys. Res*., 1987, **92,** 1337–1347.
14. Makurat, A., Barton, N., Rad, N. S. and Bandis, S., Joint conductivity variation due to normal and shear deformation. In *Proc. Int. Symp. Rock Joints*, eds. N. Barton and O. Stephansson. Balkema, Rotterdam, 1990, pp. 535–540.
15. Piggott, A. R. and Elsworth, D., Laboratory studies of transport within a single rock fracture. In *Proc. Int. Symp. Rock Joints*, eds. N. Barton and O. Stephansson. Balkema, Rotterdam, 1990, pp. 397–404.
16. Amadei, B. and Illangasekare, T., Analytical solutions for steady and transient flow in non-homogeneous and anisotropic rock joints. *Int. J. Rock Mech. Min. Sci. Geomech. Abstr*., 1992, **29,** 561–572.
17. Esaki, T., Nakahara, K., Jiang, Y. and Mitani, Y., Effects of preceding shear history on shear-flow coupling properties of rock joints. In *Mech. of Jointed and Faulted Rock*, eds. H.-P. Rossmanith. Balkema, Rotterdam, 1995, pp. 501–506.
18. Zimmerman, R. W. and Bodvarsson, G. S., Hydraulic conductivity of rock fractures. *Transport Porous Media*, 1996, **23,** 1–30.
19. Walsh, J. B., Effect of pore pressure and confining pressure on fracture permeability. *Int. J. Rock Mech. Min. Sci. Geomech. Abstr*., 1981, **18,** 429–435.
20. Barton, N. S., Bandis, S. and Bakhtar, K., Strength, deformation and conductivity coupling of rock joints. *Int. J. Rock Mech. Min. Sci. Geomech. Abstr*., 1985, **22,** 121–140.
21. Pyrak-Nolte, L. J., Nolte, D. D., Myer, L. R. and Cook, N. G. W., Fluid flow through single fractures. In *Proc. Int. Symp. Rock Joints*, eds. N. Barton and O. Stephansson. Balkema, Rotterdam, 1990, pp. 405–412.
22. Olsson, W. A. and Brown, S. R., Hydromechanical response of a fracture undergoing compression and shear. *Int. J. Rock Mech. Min. Sci. Geomech. Abstr*., 1993, **30,** 845–851.
23. Raven, K. G. and Gale, J. E., Water flow in a natural rock fracture as a function of stress and sample size. *Int. J. Rock Mech. Min. Sci. Geomech. Abstr*., 1985, **22,** 251–261.
24. Sundaram, P. N., Watkins, D. J. and Ralph, W. E., Laboratory investigations of coupled stress-deformation-hydraulic flow in a natural rock fracture. In *Proc. 28th U.S. Symp. Rock Mech*., eds. I. Farmer, J. Daemen, C. Desai, C. Glass and S. Neuman. Balkema, Rotterdam, 1987, pp. 585–592.
25. Durham, W. B. and Bonner, B. P., Closure and fluid flow in discrete fractures. In *Fractured and Jointed Rock Masses*, eds. L. R. Myer, N. G. W. Cook, R. E. Goodman and C.-F. Tsang. Balkema, Rotterdam, 1995, pp. 441–446.
26. Gentier, S., Lamontagne, E., Archambault, G. and Riss, J., Anisotropy of flow in a fracture undergoing shear and its relationship to the direction of shearing and injection pressure.. *Int. J. Rock Mech. Min. Sci. Geomech. Abstr.(Paper No. 094)*, 1997, **34,** 3–4.
27. Yeo, I. W., Anisotropic hydraulic properties of a rock fracture under normal and shear loading. Ph.D. thesis, University of London (Imperial College), London, U.K., 1997.
28. Hakami, E., Aperture distribution of rock fractures. Ph.D. thesis, Royal Institute of Technology, Stockholm, Sweden, 1995.
29. Bandis, S. C., Lumsden, A. C. and Barton, N. R., Experimental studies of scale effects on the shear behaviour of rock joints. *Int. J. Rock Mech. Min. Sci. Geomech. Abstr*., 1981, **18,** 1–21.
30. Iwai, K., Fundamental studies of fluid flow through a single fracture. Ph.D. thesis, University of California, Berkeley, 1976.
31. Iwano, H. and Einstein, H. H., Stochastic analysis of surface roughness, aperture and flow in a single fracture. In *Proc. Int. Symp. EUROCK '93*, eds. L. Ribeiro e Sousa and N. F. Grossmann. Balkema, Rotterdam, 1993, pp. 135–141.
32. Clark, I., *Practical Geostatistics*. Elsevier Applied Science Publishers, London, 1976.
33. Pannatier, Y., MS-Windows programs for exploratory variography and variogram modelling in 2D. In *Statistics of Spatial Processes: Theory and Applications*, Bari, Italy, Sept. 27–30, 1993, pp. 225–231.
34. Zienkiewicz, O. C. and Taylor, R. L., *The Finite Element Method*. McGraw-Hill, U.K., 1991.
35. Istok, J., *Groundwater Modeling by the Finite Element Method*. American Geophysical Union, Washington, 1989.
36. Todd, D. K., *Groundwater Hydrology*. John Wiley and Sons, New York, 1980.
37. Wittke, W., *Rock Mechanics*. Springer-Verlag, Berlin, 1990.
38. de Marsily, G., *Quantitative Hydrogeology*. Academic Press, San Diego, 1986.
39. Hasegawa, E. and Izuchi, H., On steady flow through a channel consisting of an uneven wall and a plane wall. Part 1. Case of no relative motion in two walls. *Bull. Jpn. Soc. Mech. Eng*., 1983, **26,** 514–520.
40. Zimmerman, R. W., Kumar, S. and Bodvarsson, G. S., Lubrication theory analysis of the permeability of rough-walled fractures. *Int. J. Rock Mech. Min. Sci. Geomech. Abstr*., 1991, **28,** 335–341.
41. Mourzenko, V. V., Thovert, T.-F. and Adler, P. M., Permeability of a single fracture: validity of the Reynolds equation. *J. Phys. II*, 1995, **5,** 465–482.